Geochemistry, Geophysics, Geosystems®

RESEARCH ARTICLE
10.1029/2022GC010376

Greigite (Fe_3S_4) Formation in Artificial Sediments via Solid-State Transformation of Lepidocrocite

Sophie C. Roud[1], Stuart A. Gilder[1], and SoHyun Park[1]

[1]Department of Earth and Environmental Sciences, Ludwig Maximilian University of Munich, Munich, Germany

Key Points:

- We present a new method to grow greigite in aqueous sediments and create a chemical remanent magnetization under controlled conditions
- Greigite grain sizes of 20–50 nm span the superparamagnetic to single domain threshold, consistent with theoretical predictions
- Our experimental hysteresis data coincide with calculated mixing curves allowing better quantification of greigite particle sizes in nature

Correspondence to:

S. C. Roud,
sophie.roud@lmu.de

Citation:

Roud, S. C., Gilder, S. A., & Park, S. (2022). Greigite (Fe_3S_4) formation in artificial sediments via solid-state transformation of lepidocrocite. *Geochemistry, Geophysics, Geosystems*, *23*, e2022GC010376. https://doi.org/10.1029/2022GC010376

Received 3 FEB 2022
Accepted 22 JUN 2022

Author Contributions:

Conceptualization: Sophie C. Roud
Formal analysis: Sophie C. Roud, SoHyun Park
Funding acquisition: Sophie C. Roud, Stuart A. Gilder
Investigation: Sophie C. Roud
Methodology: Sophie C. Roud
Supervision: Stuart A. Gilder
Visualization: Sophie C. Roud
Writing – original draft: Sophie C. Roud
Writing – review & editing: Sophie C. Roud, Stuart A. Gilder, SoHyun Park

Abstract Greigite (Fe_3S_4) is a ferrimagnetic iron-sulfide mineral that forms in sediments during diagenesis. Greigite growth can occur diachronously within a stratigraphic profile, complicating or overprinting environmental and paleomagnetic records. An important objective for paleo- and rock-magnetic studies is to identify the presence of greigite and to discern its formation conditions. Greigite detection remains, however, challenging and its magnetic properties obscure due to the lack of pure, stable material of well-defined grain size. To overcome these limitations, we report a new method to selectively transform lepidocrocite to greigite via the intermediate phase mackinawite (FeS). In-situ magnetic characterization was performed on discrete samples with different sediment substrates. Susceptibility and chemical remanent magnetization increased proportionally over time, defining two distinct greigite growth regimes. Temperature dependent and constant initial growth rates indicate a solid-state FeS to greigite transformation with an activation energy of 78–90 kJ/mol. Low and room temperature magnetic remanence and coercivity ratios match with calculated mixing curves for superparamagnetic (SP) and single domain (SD) greigite and suggest ~25% and ~50% SD proportions at 300 and 100 K, respectively. The mixing trend coincides with empirical data reported for natural greigite-bearing sediments, suggesting a common SP endmember size of 5–10 nm that is likely inherited from mackinawite crystallites. The average particle size of 20–50 nm determined by X-ray powder diffraction and electron microscopy accords with theoretical predictions of the SP/SD threshold size in greigite. The method constitutes a novel approach to synthesize greigite and to investigate its formation in sediments.

Plain Language Summary Sediments provide continuous records of Earth's ancient magnetic field, which lend insights into the workings of the geodynamo and help to establish the geologic time scale through global magnetostratigraphic correlation. Greigite is a magnetic iron sulfide mineral that commonly forms after deposition, thereby remagnetizing the sediment and complicating interpretation of the magnetic record. Understanding greigite formation and detecting its presence is fundamental for obtaining reliable records of the paleomagnetic field, yet knowledge of how greigite grows and how its magnetic properties evolve during growth remains limited. This article outlines a novel approach to form greigite in sediments and to monitor its growth kinetics, grain size and magnetic remanence acquisition. The magnetic properties of the synthetic sediments resemble those of natural greigite-bearing sediments and match well with theoretical calculations, which can help quantify grain sizes in sedimentary greigite. The reported method and our results contribute to a better understanding of greigite formation and chemical magnetic remanence acquisition in sediments.

1. Introduction

Greigite, the sulfide analog of magnetite, is a common authigenic magnetic mineral that forms at the expense of existing iron-rich mineral phases during diagenetic processes in sediments. Formation of greigite is of interest for paleomagnetic studies, because it can lead to a secondary chemical remanent magnetization (CRM) that is younger than the stratigraphic age of the sediment and can bias or overprint the primary paleomagnetic record (Hallam & Maher, 1994; Jiang et al., 2001; Just et al., 2019; Larrasoaña et al., 2007; Nowaczyk et al., 2020; Roberts et al., 2005; Ron et al., 2007; Rowan & Roberts, 2006; Sagnotti et al., 2005). Multiple generations of greigite can grow at any time after deposition if favorable conditions exist in a sediment (Roberts & Weaver, 2005). Understanding, greigite formation conditions, its magnetic properties and the characteristics of a CRM are crucial for paleomagnetic studies to determine whether the magnetic remanence is primary, secondary or a mix of the two.

Aside from remagnetizing sediments, greigite is relevant as a potential catalyst for the emergence of life (White et al., 2015) and plays a role in geochemical sulfur and iron cycles as an intermediate phase in the pyritization process (Hunger & Benning, 2007). Greigite is, however, not a necessary precursor of pyrite (FeS_2), as originally

proposed (Schoonen, 2004) and its preservation is now thought to inhibit pyrite formation. Greigite formation requires preexisting mackinawite (FeS), which oxidizes to Fe_3S_4 in a solid-state transformation, whereas pyrite forms from dissolved sulfide species (Rickard, 2012). Compared to pyrite, natural greigite concentrations are typically low, and the conditions under which it accumulates in sediments are not fully understood. One factor for the limited understanding of natural greigite abundances is the lack of analytical geochemical techniques to identify and quantify the mineral in the bulk sediment, due to its low concentrations. Furthermore, greigite is geochemically indistinguishable from similarly reactive sulfide compounds that are part of the acid volatile sulfide fraction, such as nanoparticulate pyrite and mackinawite.

Rock-magnetic methods are ideal for characterizing small, dilute concentrations of magnetic minerals like greigite. Authigenic greigite can exhibit magnetic characteristics such as gyroremanence, multiaxial crystalline anisotropy, and strong magnetostatic interactions, which facilitate its identification, especially in the single domain (SD) state. Reliably detecting its presence and distinguishing greigite from other magnetic minerals remains challenging because proxy-parameters are often non-unique and depend on factors such as magnetic domain state, metal substitution and magnetic interactions, so that the ranges of possible values overlap, particularly between greigite and magnetite (Roberts et al., 2011). Our understanding of the magnetic properties of greigite remains incomplete; obstacles are a scarcity of pure, well characterized reference material in addition to the fact that greigite readily oxidizes under typical laboratory conditions. Moreover, it is still elusive how greigite acquires a CRM in sediments because the process has not been recreated nor investigated under controlled laboratory conditions.

To overcome these limitations, we report a novel method to synthesize greigite in sediments by a two-step transformation of lepidocrocite via the intermediate phase FeS. Greigite growth and CRM acquisition are monitored during the FeS to greigite transformation using bulk magnetic remanence and susceptibility measurements. Based on results from magnetic measurements, scanning electron microscopy (SEM) and X-ray powder diffraction (XRD) we characterize the transformation process including the growth rate, evolution of mineral phases, and their average grain sizes. The magnetic domain state, grain size and SD proportions of the synthetic greigite are determined using low and room temperature magnetic measurements, which we compare to theoretical models and empirical data for natural sedimentary greigite distributions. The objectives of this study are to document the growth process of greigite and especially the evolution in magnetic properties during its growth; remanence-related aspects will be treated separately.

2. Methods

2.1. Synthesis

Synthetic greigite samples (45 in total) were prepared by a two-step transformation of lepidocrocite. Our synthesis method partially follows the solid-gas transformation of Fe-oxides by Igarashi et al. (2016) and uses the "iron sulfide switch" of Rickard et al. (2001) for preferential transformation of FeS to greigite under controlled aqueous conditions. All reactions were performed in crimp-sealed, 10 ml glass vials (Ø22 × 40 mm) prepared under argon atmosphere within a glovebox.

2.1.1. Dry Sulfidation of Lepidocrocite (Step I)

Synthetic lepidocrocite (γ−FeOOH, grain size <200 nm, Bayferrox® 943) was sulfidized by exposure to hydrogen sulfide gas. To achieve this, 22 mg (0.25 mmol) of dry, nanocrystalline γ −FeOOH powder was placed into sample vials together with a quartz glass tube containing 0.5 ml of 1M Na_2S. After the vials were sealed with rubber stoppers, 0.5 ml of 2M HCl were injected into the tubes, neutralizing the Na_2S solution and releasing H_2S gas. This led to an immediate blackening (sulfidation) of the initially yellow lepidocrocite powder. The concentration of reactants was chosen to produce an excess of sulfide (0.5 mmol) over iron (0.25 mmol). After aging the samples in a H_2S atmosphere at room temperature for 15 hr, the vials were briefly opened inside the glove box to remove the quartz glass tube and weigh the transformation product.

2.1.2. Aging in Aqueous Solution (Step II)

The aging solution was prepared in 250 ml glass bottles from degassed, demineralized water supplemented with resazurin as a redox indicator. The redox potential was poised below $E_h = -51$ mV (as indicated by the reduction of blue resazurin to purple resorufin) by adding sodium sulfide (Na_2S) to a final concentration of 20 mM,

Table 1
Mass Balance for Step I, the Anhydrous Transformation of Lepidocrocite (γ−FeOOH) to FeS + H_2O (Product I), Together With Aging Conditions and Magnetic Susceptibility Data for Step II, the Transformation of Product I to Greigite and Mackinawite (Product II)

		Step I		Step II					
		Reactant	Product I	Substrate		Aging conditions		Product II	
Sample id	n	γ−FeOOH (mg)	FeS + H_2O (mg)	V (cm³)	Grain size	t (h)	B_0 (μT)	κ_{lf} ($\times10^{-5}$)	κ_{fd} (%)
#100-03 to #100-09	7	22	29.8 (1.7)	3	Sand	7	100	105.8 (4.9)[a]	7.5 (0.7)[a]
#100-10 to #100-16	7	22	30.3 (1)	3	Silt	7	100	103.4 (6.2)[a]	7.4 (0.5)[a]
#100-02	1	22	30.3	-	-	7	100	99.1	6.5
#50-17 to #50-23	7	22	29.8 (1.2)	3	Sand	6	50	99.0 (6.5)	7.7 (0.7)
#50-24 to #50-30	7	22	31 (1.2)	3	Silt	6	50	88.5 (8.1)	7.6 (1.3)
#50-31	1	22	32.3	-	-	6	50	107.9	7.8
#25-33 to #25-39	7	22	30 (0.7)[a]	3	Sand	7.5	25	122.4 (13.0)	7.1 (0.5)
#25-41 to #25-47	7	22	30.1 (0.3)[a]	3	Silt	7.5	25	110.6 (6.2)	7 0.0 (0.4)
#25-48	1	22	30	-	-	7.5	25	136.8	6.1

Note. Mean values and standard deviation (in parentheses) of sample masses, low frequency bulk susceptibility (κ_{lf}) and frequency-dependent susceptibility (κ_{fd}) for groups of equally treated samples; $n = 7$ unless otherwise stated.

[a]indicates $n = 6$. #100, #50, and #25 in the sample IDs indicate the applied magnetic field value in μT.

which resulted in a dissolved sulfide amount of 0.1 mmol per 5 ml sample. Formaldehyde (HCHO) was added to a concentration of 50 mM to promote greigite and inhibit pyrite formation in the sulfidic solution (Rickard et al., 2001). The pH was adjusted to 5.5 with HCl.

Freshly prepared reaction products from Step I were either directly suspended in 5 ml aging solution or initially dispersed in a non-magnetic silica substrate and then suspended in the aging solution. For the latter, two grain sizes were used: either 5 g of 100–400 μm quartz sand (Carl Roth GmbH) or 3 g of 2–40 μm SiO_2 powder (Alfa Aesar), respectively, that are referred to as sand and silt. After mixing and settling overnight, matrix-bearing samples had a sediment volume of 3 cm³. Based on the bulk and grain densities, ρ (ρ_{sand} = 1.67 g/cm³, ρ_{silt} = 1.00 g/cm³ and ρ_{silica} = 2.65 g/cm³), porosities of 37% and 67% were estimated for the sand and silt samples, respectively. In silt samples the Fe-fraction and matrix grains formed a homogenous sediment slurry, whereas in sand samples most of the Fe-fraction deposited on top of sand grains.

The vials were placed in a non-magnetic incubator at 75°C that was housed in Helmholtz coils to control the strength and direction of the magnetic field during aging. The incubator consisted of a thermally insulated aluminum block with cavities that accommodated 16 vials. Temperature was monitored with a thermometer placed inside one dedicated vial. The setup provided uniform magnetic field and temperature conditions in which the samples reached the set temperature within a few minutes. Three separate experiments were carried out in magnetic field strengths of 100 μT, 50 μT, and 25 μT (batch #100, #50, and #25) with a constant field direction of declination, $D = 0°$ and inclination, I = 45°. Each experiment consisted of 15 vials: seven with a sand matrix, seven with a silt matrix and one without matrix (Table 1).

2.2. Analytical Methods

Powder X-ray diffraction (XRD) was performed with a STOE diffractometer (STADI P) with Mo$K_{\alpha1}$ radiation (wavelength = 0.7093 Å; Ge(111) monochromator). Wet synthesis products were freeze-dried and sealed between layers of Kapton tape under argon atmosphere to prevent oxidation. Phase identification of XRD data was based on the Crystallography Open Database (Gražulis et al., 2012) using the Match! v3.11 software package (Crystal Impact).

Secondary electron and backscattered electron images were acquired using a Hitachi SU5000 field emission scanning electron microscope (SEM) operating at 10 kV. SEM samples were prepared in an argon atmosphere from the same bulk materials used for X-ray diffraction; dry powder was placed on carbon pads and was carbon

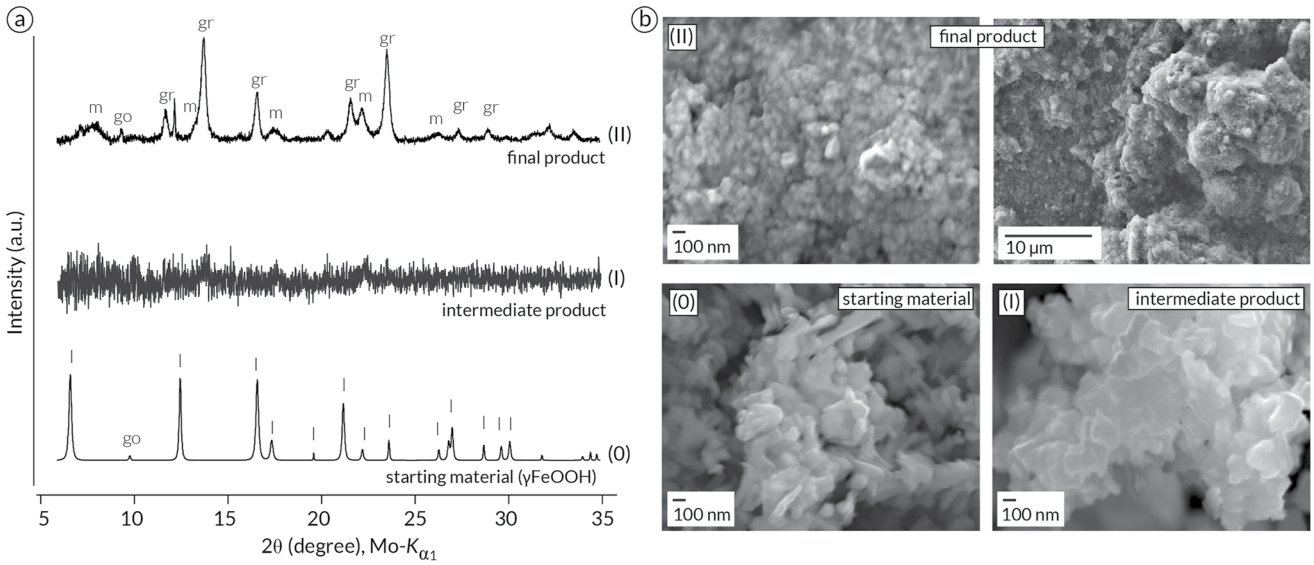

Figure 1. Starting material and transformation products. (a) XRD data and (b) SEM images of the starting material γ−FeOOH (0), the intermediate product (Step I) and the final product (Step II). The XRD pattern of the starting material indicates that lepidocrocite (l) is the main phase along with trace amounts of goethite (go). The XRD pattern for the sample from Step II has reflections of greigite (gr) and mackinawite (m) as the main phases.

coated (8 nm-thick). Particle sizes were determined from 12.5 µm^2 images using the software ImageJ (Schneider et al., 2012). The particle area, A was measured at 50,000-fold magnification; the average grain diameter, d was estimated as $d = 2\sqrt{A/\pi}$ assuming a circular footprint.

Room temperature magnetic susceptibility, κ, was measured before and after 75°C aging with a MS2B Bartington Instruments susceptibility meter at two frequencies (low-frequency, lf = 465 Hz and high-frequency, hf = 4,650 Hz) to calculate the frequency-dependence of susceptibility, $\kappa_{fd} = 100\,(\kappa_{lf} - \kappa_{hf})/\kappa_{lf}$. Low-frequency susceptibility, κ_{lf} was monitored in 20 min intervals during the heating experiment on a subset of four samples. For these four, the vials were briefly removed from the heat and immediately measured without cooling to room temperature (measurement temperature 50–70°C). The remanent magnetization was measured on the same subset of samples in 1–2 hr intervals during the aging process using a vertical 2G Enterprises Inc., three axis, superconducting magnetometer housed in a magnetically shielded room (residual field <500 nT). Each of the four sample vials was measured in two positions using a custom, manual sample handler and then returned to the aging set-up within minutes. The manual hander allowed careful lowering of the vials into the magnetometer and to rotate them about a vertical axis between consecutive measurements with minimal disturbance of the sediment slurry.

Hysteresis loops, backfield demagnetization, and first-order reversal curves (FORCs) were measured with a Princeton Measurements Corporation vibrating sample magnetometer (VSM) at both 300 and 100 K in a nitrogen atmosphere. To monitor magnetic properties during progressive sample oxidation, a series of 20 room temperature FORCs was measured in air (sample #100-10) over 12 hr. VSM sub-samples were prepared in an argon atmosphere from freeze-dried bulk materials; dry sand and silt samples (#100-03 and #100-10) were pressed into gel caps and pure sulfide powder (#50-31) was fixed with Kapton tape. Saturation fields of 300 mT were used for all experiments. FORC settings were optimized for short measurement times to minimize drift and sample oxidation (B_u = −50/+30 mT, B_c = 0–100 mT, B_{sat} = 300 mT, 1 or 2 mT increment [N = 93 or 173], 150 ms averaging time). FORC data were processed using FORCinel v3.06 (Harrison & Feinberg, 2008) with subtraction of the lower branch of the hysteresis envelop and using VARIFORC smoothing (Egli, 2013). Hysteresis, backfield and FORC measurements were used to calculate the ratio of saturation remanent magnetization over saturation magnetization M_{rs}/M_s and the coercivity of remanence over coercivity B_{cr}/B_c as proxies for magnetic domain state.

Day plot (Day et al., 1977) mixing curves for SD and superparamagnetic (SP) greigite were calculated following Dunlop (2002, Equation 5 and 6) with $M_{rs}/M_s = f_{SD}(M_{rs}/M_s)_{SD}$ and $B_{cr}/B_c = (B_{cr})_{SD}/(B_c)_{SD}[f_{SD}\chi_{SD}/(f_{SD}\,\chi_{SD} + f_{SP}\,\chi_{SP})]$ using greigite room temperature SD endmember values of $(M_{rs}/M_s)_{SD}$ = 0.866 (Winklhofer et al., 2014), $(B_{cr})_{SD}$ = 90 mT and $(B_c)_{SD}$ = 75 mT (Chang et al., 2009, Figure 1). M_s = 272 kA/m (Li et al., 2014) applies to

the greigite SD and SP state, while B_{cr}, B_c and M_{rs} are zero for SP grains. f_{SD} and f_{SP} are the fractions of SD and SP grains, respectively, and χ_{SD} and χ_{SP} are the respective initial susceptibilities, where $\chi_{SD} = (M_{rs})_{SD}/(B_c)_{SD}$. $\chi_{SP} = \mu 0 V M_s^2/3k_bT$, where μ_0 is vacuum permeability, and k_b the Boltzmann constant, was calculated for temperature, $T = 300$ K and volume, V for cubic grains of diameters, $d = 5$ and 10 nm.

3. Results

3.1. Transformation Reactions and Material Characterization

3.1.1. Starting Material

XRD data confirmed that the starting material consists mainly of nano-crystalline lepidocrocite with minor goethite impurities (α−FeOOH, strongest peak at $2\theta = 9.6°$, Figure 1a). An average crystallite size of 60 nm was estimated from the full width at half maximum (FWHM) of lepidocrocite reflections ($2\theta = 6$–$20°$) using the Scherrer equation (Scherrer, 1912). SEM images of the synthetic lepidocrocite sample contain elongated platelets of crystalline aggregates with an average size of 110 ± 37 nm ($N = 50$ grains) (Figure 1b).

3.1.2. Transformation Step I

Exposing lepidocrocite to H_2S gas at room temperature led to a blackening of the initially yellow powder, which is indicative of sulfidation. Like the starting material, the black transformation product after 15 hr was not attracted to a neodymium magnet and the magnetic susceptibility was below detection limits (within $\pm 1 \times 10^{-5}$ SI), which indicates transformation to a non-magnetic Fe-sulfide. The average sample weight increased by 8 ± 1 mg (± single standard deviation) after the transformation ($N = 45$). If sulfidation caused the weight increase, this suggests an added sulfur amount of 0.25 mmol per sample, that is, the addition of one mol of sulfur per mole of FeOOH. XRD data for the transformation product lack well-defined diffraction-peaks (Figure 1a, middle row), which points to a complete transformation of the Fe-oxyhydroxide to an X-ray amorphous phase. SEM images of the transformation product show agglomerates of platy, 100–200 nm particles, slightly larger and more rounded than the starting material (Figure 1b). Image analysis indicates an average grain diameter of 155 ± 43 nm ($N = 50$ grains).

3.1.3. Transformation Step II

After the dry black transformation product of Step I was suspended in the aging solution, the initially pink solution became transparent over time, indicating a reduction of resorufin and concomitant lowering of the redox potential to below $E_h = -110$ mV. In samples where the black powder was in direct contact with the solution (samples without matrix and with sand matrix), the pink color began fading immediately, and the solution turned transparent within 1 hr. In silt samples, where the black powder was embedded in the silica matrix, the color change was noticeably slower (the solution became transparent overnight). This suggests that the initial reaction kinetics depend on the exposure of the Fe-fraction to the aging solution.

Approximately 1 hr after sample preparation at room temperature, the magnetic susceptibility of all samples from batch #100 increased slightly to 2.4 (±1.0)×10^{-5} (dimensionless SI unit, normalized by the vial volume of 10 cm³; $n = 15$). Susceptibility more than doubled to 5.7 (±1.5) × 10^{-5} within 15 hr aging. In total, 29 of 45 samples had susceptibilities above the noise level after 15 hr at room temperature ($\overline{\kappa_{lf\#50}} = 9.2$ (±4.6) × 10^{-5}, $n = 12$; $\overline{\kappa_{lf\#25}} = 2.0$ (±1.0) × 10^{-5}, $n = 2$). The overall average susceptibility at this stage was 6.9 (±3.8) × 10^{-5} with an average frequency dependency of 21 ± 6% ($n = 29$).

Susceptibility increase during aging experiments at 75°C is shown in Figure 2a for representative sand and silt samples (#100-03, -04, -10 and -11). For all samples, κ_{lf} rose immediately upon heating and kept increasing throughout the experiment, reaching a value of 96.6 (±4.8) × 10^{-5} after 6 hr. In Figure 2b, normalized and averaged growth curves demonstrate a consistent time-dependent behavior among the samples (single standard deviation <4%) with a distinct change in growth rate at 2 hr aging time.

Like susceptibility, the natural remanent magnetization (NRM) of the same four samples increased over time, reaching 130 (±10) mA/m (normalized to the vial volume of 10 cm³) after 7 hr (Figure 2c). The magnetization changed less than 3% after storing the samples in a magnetically shielded room for 12 hr and remeasuring the NRM. Magnetization and susceptibility increased linearly with time (Figure 2d), indicating a high degree of proportionality during greigite growth; NRM/κ_{lf} was 1.3 mA/m for silt samples and 1.2 mA/m for sand samples.

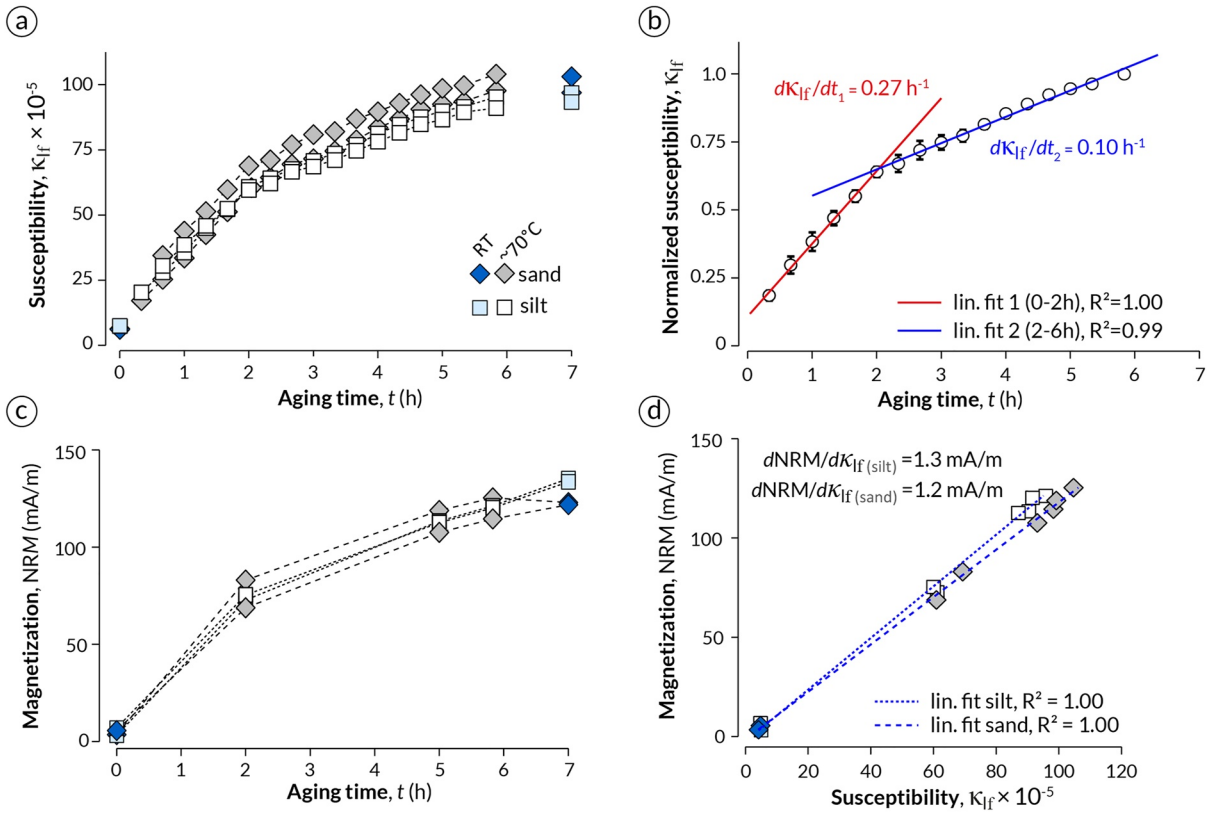

Figure 2. Greigite growth and grain size characterization. (a) Low-frequency magnetic susceptibility κ_{lf} against aging time (t, in hours). Measurements during the experiment (gray and open symbols) were performed on samples close to 70°C; the initial and final data points (blue) were measured at room temperature. (b) Mean and standard deviation ($n = 4$) of normalized κ_{lf} curves with average susceptibility growth rates $d\kappa_{lf}/dt$. (c) Natural remanent magnetization, NRM against aging time (t, in hours). (d) NRM against κ_{lf} demonstrating a linear correlation ($R^2 = 1.00$) among sand and silt samples. A magnetic field of 100 μT was applied in all cases. Diamonds and squares represent sand (#100-03 and -04) and silt samples (#100-10 and -11), respectively.

XRD patterns for a sample aged for 6 hr at 75°C (sample #50-31 without silica matrix) indicate the presence of nano-crystalline greigite and mackinawite (FeS) with minor contributions of goethite and a hydrous iron sulfate (powder diffraction file 00-009-0006; highest peak at $2\theta = 12.13$) (Figure 1a, upper row). Quantitative analysis based on the respective peak intensities and molecular weight of the two main phases yields mass fractions of 62% Fe_3S_4 and 38% FeS_m. Semi-quantitative analysis of the aging solutions (QUANTOFIX® Iron 100 test swabs) suggests total dissolved iron concentrations >100 mg/l (2 mM) at the end of Step II heating experiments. 100 mg/l was the upper detection limit of the test swabs, which, from the solution volume of 5 ml, is equivalent to 0.5 mg or 4% of the total iron per sample.

From peak-broadening in the XRB pattern of sample #50-31, we could estimate respective average crystallite sizes of 20 and 10 nm for Fe_3S_4 and FeS. SEM images of the sample taken at the highest possible resolution (Figure 1b) indicate that individual grains are close to or below the resolution limit and substantially smaller than the lepidocrocite starting material. Image analysis yields an average grain diameter of 51 ± 14 nm ($N = 200$ grains). However, as smaller grains could not be resolved in detail, the estimate is likely biased toward larger grain sizes. SEM images at lower magnifications indicate that the particles cluster in a fractal manner into aggregates with sizes up to ~10 μm.

3.2. Final Bulk Magnetic Susceptibility

The final (room temperature) susceptibility averaged 105.6 (±13.8) × 10^{-5} with a frequency dependence of 7.3 ± 0.8% ($n = 43$). The average susceptibility values for different matrix types are shown in Figure 3. Systematic differences in susceptibility and its frequency dependence among batches correlate with aging time (Pearson correlations: κ_{lf} ~ aging time: $R = 0.71$, $p < 0.001$; κ_{fd} ~ aging time: $R = -0.33$, $p < 0.01$) but not with the applied

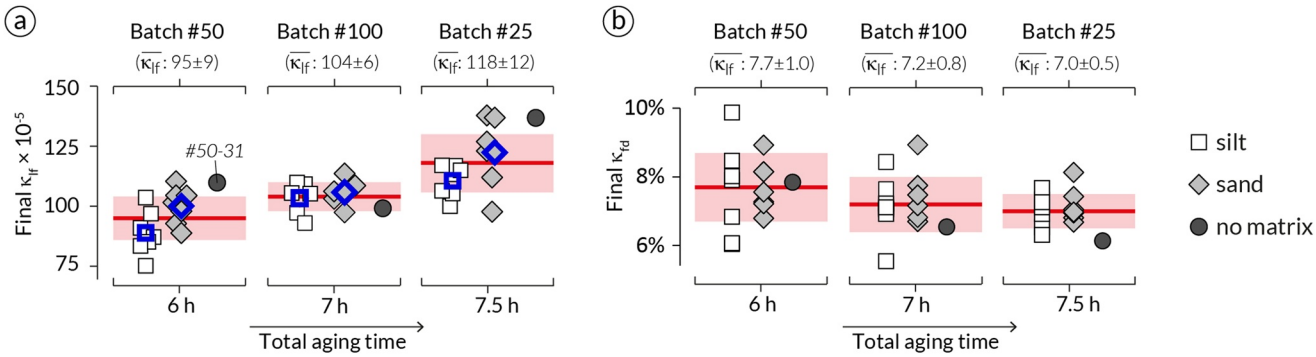

Figure 3. Final bulk susceptibility values. (a) Low frequency susceptibility κ_{lf} and (b) frequency-dependent susceptibility κ_{fd} with respect to the final (75°C) aging time for each batch and grouped by matrix type: sand (cubes), silt (diamonds) and no matrix (circles). Mean values for $\overline{\kappa_{lf}}$ and $\overline{\kappa_{fd}}$ and their standard deviations are indicated in red for each batch. Blue symbols in (a) indicate individual group means.

magnetic field strength. Samples with sand matrices tended to have higher susceptibilities than those with silt for each batch; however, independent *t*-tests suggest that the difference is only statistically significant for batch #50 (t[2.4] = 11, $p = 0.02$, $\overline{\kappa_{lf-sand}} = 99 \pm 7 \times 10^{-5}$, $\overline{\kappa_{lf-silt}} = 88 \pm 9 \times 10^{-5}$).

3.3. Magnetic Characterization at Low and Room Temperature

To better characterize the magnetic domain state of the material, the remanence and coercivity ratios, M_{rs}/M_s and B_{cr}/B_c, were determined for one sample of each sediment type (#100-03 and #100-10) and a pure sulfide sample (#50-31, which was also analyzed by XRD and SEM) at 300 and 100 K. The results are shown in Figure 4a

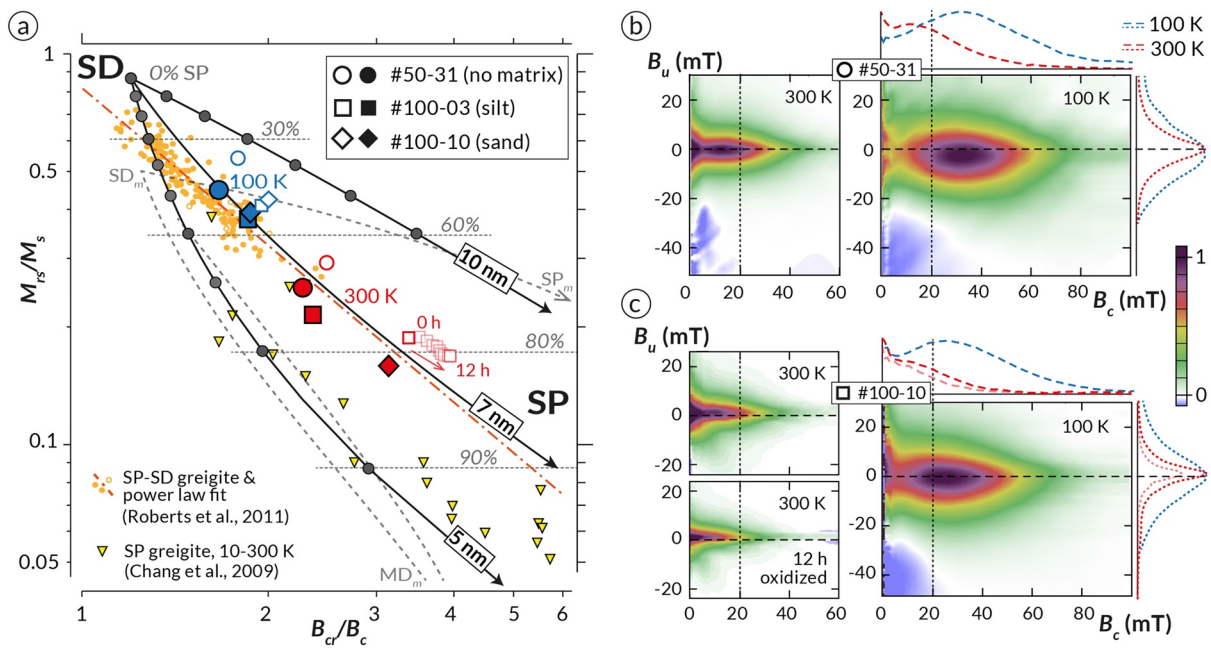

Figure 4. Magnetic properties of representative samples at 300 and 100 K. (a) Remanence (M_{rs}/M_s) versus coercivity (B_{cr}/B_c) ratios determined from hysteresis and backfield curves (filled symbols) and FORCs (open symbols); pink squares indicate the progressive oxidation in air over ~12 hr. Solid black lines represent calculated single domain (SD) and superparamagnetic (SP) mixing curves for greigite (Section 2.2). For reference, the SD to multidomain (MD) and SP(10 nm)-SD mixing curves for uniaxial magnetite (Dunlop, 2002) are shown as gray dashed lines. Yellow symbols indicate data for natural SP-SD greigite-bearing sediments (solid circles), synthetic samples (open circles Dekkers & Schoonen, 1996) and a power law fit (Roberts et al., 2011); yellow triangles represent natural SP greigite measured between 5 and 300 K (Figure 1 of Chang et al., 2009, samples NR08 and NR27). (b and c) FORC diagrams for sample #50-31 (no matrix) and #100-10 (silt matrix) at 300 K (left) and 100 K (right). Colored, dashed lines (blue = 100 K, red = 300 K) represent the horizontal and vertical distribution of FORC amplitudes along $B_u = 0$ mT and $B_c = 20$ mT, respectively (black dashed lines). Pink dashed lines in (c) represent measurements after exposing the sample to air for 12 hr.

together with theoretical SP-SD mixing lines for greigite that were calculated as described in Section 2.2. Our measured data lie within an envelope confined by SP endmembers of 5 and 10 nm. Their distribution roughly coincides with a 7 nm SP mixing line as well as with an empirical greigite mixing line reported by Roberts et al. (2011). The latter represents a power-law fit to the compiled experimental data from the literature for greigite-bearing sediments (n = 181) and synthetic (n = 9) samples. Hysteresis ratios reported for natural SP greigite between 5 and 300 K (Chang et al., 2009) have a similar temperature dependency and follow our calculated 5 nm SP mixing line. M_{rs}/M_s ratios for our samples correspond to calculated SP volume fractions of 76 ± 4% (n = 3) at 300 K and are shifted toward the SD endmember with SP proportions of 53 ± 3% (n = 3) at 100 K.

FORC diagrams measured at 300 K (Figure 4b) contain horizontal signatures with a bimodal coercivity distribution. Peak amplitudes at $B_c = 0$ indicate thermally activated grains close to the SP-SD threshold (Pike et al., 2001). A wider maximum at 12 mT is characteristic of more stable SD grains (coercivity distributions along $B_u = 0$ are shown for 300 and 100 K in Figure 4b). The vertical spread of the FORC distribution indicates magnetostatic interactions among grains (Pike et al., 1999). The amount of vertical spread is strongest close to the origin and generally scales with the FORC amplitude along the ridge. Room temperature oxidation of the silt sample shifts the FORC distribution toward the origin and reduces the intensity and vertical spread. Remanence and coercivity ratios extracted from the FORC data are comparable to those determined from hysteresis and backfield curves, although values from the FORC data are offset upward and to the right on the Day diagram (Figure 4a). Day plot ratios for the silt sample left in an open-air atmosphere at 300 K shift progressively toward more SP-like values over time (Figure 4a).

FORCs at 100 K also have bimodal coercivity distributions with one narrow maximum close to the origin and a broader maximum at 25–30 mT (B_c) (Figure 4b, right). Lowering the temperature from 300 to 100 K, increases the coercivity. The vertical spread defined by the FWHM (full width at half-maximum) of the vertical FORC distributions at B_c = 20 mT increased from 10 mT at 300 K to 24 mT at 100 K (Figure 4b), which indicates stronger magnetostatic interactions at 100 K. More negative B_u distributions at 100 K compared to 300 K (shift from 0 to −2 mT in #50-32 and from +2 to 0 mT in #100-10) (Figure 4b) indicate a change in the mean interaction field (Pike et al., 1999).

4. Discussion

4.1. Greigite Formation Pathway

Exposing lepidocrocite to H_2S gas during Step I produced a black, non-magnetic, X-ray amorphous material. These characteristics together with an average mass increase of one sulfur equivalent per mol of iron suggests that the iron-oxyhydroxide was reduced and sulfidized by H_2S to low-crystalline iron-monosulfide. Absence of well-defined diffraction peaks is common in freshly precipitated, nanocrystalline FeS with ∼5 nm particle sizes (Ohfuji & Rickard, 2006). In contrast to the apparently minute crystallite size of FeS, SEM images of the material indicate an average particle size of ∼150 nm, which represents a ∼40% increase with respect to the γ−FeOOH stating material. This suggests that the solid-state transformation (i.e., dehydroxylation) led to internal fragmentation of the particles, and that the seemingly larger particles seen in SEM images represent aggregates of smaller FeS regions. Similar observations were reported for the dehydroxylation of lepidocrocite to Fe-oxides by Till et al. (2014).

Assuming a complete transformation, the mass balance for Step I can be expressed as:

$$2FeOOH + 2H_2S \rightarrow 2FeS + 2H_2O + H_2. \quad (1)$$

Reduction of the aging solution during Step II was coupled to the availability of FeS (the reaction becomes slower when the sulfide is entirely embedded in the matrix), which points to FeS oxidation. Presence of dissolved iron in the aging solution at the end of Step II indicates partial dissolution of FeS and Fe release. Both observations are consistent with a solid-state transformation of the precursor FeS via loss of iron, rather than by addition of sulfur (Wilkin & Barnes, 1996) and partial oxidation of Fe^{2+} to form the mixed-valence Fe-sulfide greigite, where two-thirds of the iron is oxidized to Fe^{3+}. Although the electron acceptor (oxidizing agent) remains unclear, the respective mass balance for the transformation of FeS to Fe_3S_4 can be expressed as:

$$4Fe^{2+}S \xrightarrow{-2e^-} Fe^{2+}Fe_2^{3+}S_4 + Fe^{2+}. \quad (2)$$

The released iron fraction is expected to reprecipitate rapidly as FeS in the presence of dissolved sulfide (Rickard, 1995). Buildup of millimolar dissolved iron concentrations in the aging solution suggest that dissolved sulfide was consumed by the end of the experiment. Greigite formation occurred throughout the experiment at constant rates; therefore, H_2S was likely not involved in the oxidation of FeS, at least not in the later stage of the experiments, which may point to the autooxidation of FeS by H_2O. In preliminary experiments, identical to those described above but with pH buffered aging solutions, FeS only transformed to a magnetic phase (i.e., greigite) when the solution was briefly exposed to air or when the dry FeS was exposed to the glovebox atmosphere (0.5%–1% O_2) for several minutes. An absence of formaldehyde in the aging solution led, on the other hand, to a magnetic susceptibility decrease after some time, consistent with greigite dissolution and concomitant pyrite formation, as reported previously (Hunger & Benning, 2007; Rickard et al., 2001).

Our greigite synthesis method demonstrates that lepidocrocite can be readily sulfidized to greigite by a solid-state transformation via the precursor FeS. A similar solid-state sulfidation of hematite was reported in methanogen archaea cultures that produce extracellular bioactive greigite; moreover, equivalent abiotic transformation reactions were observed for goethite and magnetite (Igarashi et al., 2016). Direct sulfidation of Fe-(oxyhydr)oxides without prior dissolution of the precursor could represent a relevant process for greigite formation in nature when dissolved sulfide concentrations are low.

4.2. Final Greigite Concentration

Magnetic susceptibility reflects the total greigite concentration in our samples given that the susceptibilities of FeS and the silica matrix are negligible with respect to greigite. Comparable final susceptibilities (Figure 3), therefore, demonstrate that the experiments consistently facilitated greigite formation and a reproducible greigite yield, independent of the preparation method (with or without matrix). The final greigite concentration was also independent of the applied (Earth-like) magnetic field strength. Studies of hematite precipitated from ferric solutions or formed by aging ferrihydrite demonstrate a correlation with applied magnetic field intensity (Jiang et al., 2016; Stokking & Tauxe, 1990), whereas no field dependency was reported for magnetite formation by the aging of green rust (Pick & Tauxe, 1991).

XRD data analysis indicates that the crystalline solid phase of sample #100-31 consists of 62 wt% Fe_3S_4 and 38 wt% FeS (66 and 34 vol%, respectively). From the Fe_3S_4 weight fraction, Equation 2 and the initial FeS budget of 0.25 mmol per sample, a greigite mass of 13 mg is estimated for sample #100-31. The susceptibility of this sample (107.9×10^{-5}) is close to the overall mean of 105.6 ($\pm$13.8) $\times 10^{-5}$ (Figure 3a), so it is assumed that its greigite yield is representative of the entire sample set. Considering that the relative standard deviation of magnetic susceptibility is 13%, the average greigite mass in our samples is 13 $\pm$ 2 mg. For samples with a sediment matrix this converts to a greigite concentration of 1.1 $\pm$ 0.2‰ and a SD greigite concentration of 0.26 $\pm$ 0.4‰, based on the SD proportion from the Day plot (Figure 4a). The fraction of SD greigite relative to the total sulfide concentration is estimated to 16 $\pm$ 3 vol% at 300 K and 31 $\pm$ 2 vol% at 100 K.

4.3. Greigite Growth Rate

The observed reduction of the aging solution, together with a 60% susceptibility increase after the initial 15 hr aging phase at room temperature, suggests that greigite formation began as soon as FeS was submerged in the solution. Relative to the final susceptibility after the heating experiments, the susceptibility of batch #100 samples increased by 3.2 ($\pm$1.1)% between 1 and 15 hr of aging at room temperature, which can be expressed as a relative greigite growth rate of 2.3 ($\pm$0.8) $\times 10^{-3}$ hr^{-1}.

The temporal evolution of susceptibility in the 75°C aging experiment (Figure 2a) has two distinct stages with a change in slope (i.e., growth rate) at 2 hr. From the nearly linear slopes of the two segments, we determined relative greigite growth rates of 0.27 hr^{-1} and 0.09 hr^{-1} for regimes 1 and 2, respectively (Figure 2b). Linear growth rates in both stages suggest that greigite formation did not depend on the concentration of a reactant, consistent with a solid-state transformation process and with FeS to greigite transformation kinetics at aging temperatures above 125°C (Hunger & Benning, 2007). In their 125°C experiments, Hunger and Benning (2007) reported a single constant greigite growth rate; however, greigite converted to pyrite shortly after its formation, which may explain the absence of a second, slower growth period. The marked (factor of 3) rate change in our experiments could point to two distinct formation pathways or oxidizing agents, possibly related to H_2S depletion or increased

FeS crystallinity. The decrease in susceptibility and NRM growth rates may also be related to enhanced magnetostatic interactions between greigite particles, since interactions increase with particle concentration and can influence weak field magnetization processes (Egli, 2006; Muxworthy, 2001).

The room temperature growth rate was two orders of magnitude slower than the initial growth rate at 75°C. Following Hunger and Benning (2007), the initial greigite growth rates, k^{+}_{grei} determined at 25°C and 75°C were used to estimate the activation energy, E_a for the mackinawite to greigite transformation from the slope of $\ln(k^{+}_{grei})$ against $1/T$, which yields $-E_a/R$, where R is the ideal gas constant. Considering the 35% relative standard deviation of the room temperature growth rate, our E_a estimates range from 78 to 90 kJ/mol. The lower limit is in good agreement with 67.5 ± 10.6 kJ/mol as determined from the mackinawite destruction rate, k^{-}_{mack} between 100 and 200°C (Figure 4a of Hunger & Benning, 2007). Agreement between mackinawite destruction and greigite growth kinetics is expected, given a solid-state transformation between the two mineral phases. The relative growth rates and activation energy interpreted from magnetic susceptibility, thus, lie within uncertainty of those determined by XRD analyses (Hunger & Benning, 2007).

4.4. Greigite Grain Size

Average crystallite sizes determined by XRD of ~20 nm for greigite and ~10 nm for mackinawite are considered lower limits for the physical grain size because crystallite size is equal to or smaller than particle size. Minimum sizes of 10 and 20 nm accord with the average sulfide particle size of ~50 nm, as determined from SEM image analysis. The average grain size of our greigite samples, therefore, lies between 20 and 50 nm. The Fe-sulfide particle size is significantly smaller compared to the lepidocrocite starting material, for which XRD and SEM analyses yield average sizes of ~60 and ~100 nm, respectively. A smaller size of the sulfide grains is consistent with internal fracturing of lepidocrocite during the initial dihydroxylation and transformation to FeS.

Greigite grain size can be deduced indirectly from magnetic properties, which depend on magnetic domain state. Magnetic particles are in the SP state when they are too small to hold a stable magnetic remanence. Theoretical threshold sizes between the SP and SD states (relaxation time >1 min at room temperature) for greigite have been estimated to ~20 nm for interacting grain ensembles (chains of aligned, touching grains) and to ~40 nm for non-interacting ensembles (Muxworthy, 2003; Valdez-Grijalva et al., 2018; Winklhofer et al., 2014). With an average grain size between 20 and 50 nm, our samples are expected to encompass the SP/SD threshold, which is universally supported by their magnetic properties (Figures 2–4). For example, continuous acquisition of remanent magnetization during greigite growth in an applied magnetic field (Figure 2c) demonstrates the presence of stable SD grains, while the frequency dependence of susceptibility (Figure 3b) indicates that part of the greigite population is in the SP state.

SP grains detected by bulk susceptibility measured at two frequencies (465 and 4,650 Hz) have relaxation times of 0.2–2 ms. The proportion of this SP fraction relative to larger grains (with longer relaxation times) decreased from ~20% when grown at room temperature to 7% upon completion of the 75°C aging experiments (Figure 3b). This suggests that the grain size increased over time, and/or that the growth temperature influenced the final grain size. Also an increase in magnetostatic interactions, as greigite concentration increased over time, may have contributed to lowering κ_{fd} (Muxworthy, 2001). Frequency-dependent susceptibility was not measured during the 75°C experiments; however, final κ_{fd} values for the three batches correlate with total aging time (Figure 3b). Differences between the means are small (0.7% between 6 and 7.5 hr) and are not statistically significant at the 0.05 level. A relative change of SP contributions over time is also expected to affect the NRM/susceptibility ratio. Consistent with the proportional increase of the two parameters over time (Figure 2d), the average NRM/κ_{lf} ratio was constant within one standard deviation between 2 and 6 hr aging time (NRM/κ_{lf} was 1.21×10^{-8} (±4%) A/m after 2 hr and 1.25×10^{-8} (±5%) A/m after 6 hr). These observations suggest that the SP to SD ratio, and thus the average greigite particle size, did not change substantially during the 75°C aging experiments. Differences in SP contributions before and after the 75°C experiments were, therefore, restricted to the earliest growth phase and are possibly related to growth temperature.

4.5. Domain State and SD Threshold Size

FORC and hysteresis properties determined at ambient and low temperatures help to further characterize the domain state and SP/SD threshold size of our samples. Room temperature FORC diagrams are dominated by

low coercivity horizontal signatures (Figure 4b) that are characteristic of moderately interacting distributions of thermally activated SD grains close to the SP/SD threshold (Egli, 2021; Pike et al., 2001) and resemble FORC distributions of SP-dominated synthetic and natural greigite bearing samples (Roberts et al., 2006; Rowan & Roberts, 2006). Cooling to 100 K increases the coercivity and vertical spread of the FORC distributions and shifts them to lower Bu values, consistent with a decrease in thermal activation and increase in magnetic interactions (Pike et al., 2001). Overall, our 100 K FORC diagrams resemble those of natural SD greigite-bearing sediments, albeit with lower coercivities (Roberts et al., 2006, 2011). The absence of significant multi- or pseudo single domain (vortex state) signatures in the FORC diagrams indicates that the samples contain mainly SP and SD grains, which makes the calculated SP-SD mixing lines, in Figure 4a applicable to our greigite particle system. This suggests the presence of 70%–80% SP contributions at ambient temperature and approximately equal SP and SD contributions at 100 K. Cooling, thus, shifts the SP/SD threshold toward smaller grain sizes (i.e., it brings the greigite particle distribution closer to a stable SD state), as expected.

To better assess the influence of temperature on the proportions of SP and SD grains, we compared the theoretical SP/SD threshold (relaxation time, $\tau = 1$ min) for non-interacting greigite particles at 350 K (the growth temperature), 300 and 100 K. Following Winklhofer et al. (2014) and using $\tau = \tau_0 \exp\left[\left(\frac{-K_1}{12} - \frac{-K_2}{27}\right)\frac{V_b}{k_b T}\right]$ with anisotropy constants K_1 and K_2 of -16, and -6 kJ/m³ respectively, we calculated the blocking volumes, V_b and respective SP/SD threshold sizes. For spherical grains the estimated SP/SD threshold at 350, 300, and 100 K decreases from 53 to 50 to 35 nm, and for cubic grains it decreases from 43 to 40–28 nm, respectively. Differences in the stable SD grain population between growth and room temperatures are minimal. Between 300 and 100 K the SD threshold size is lowered by ~30%, which generally agrees with the observed increase in stable SD grains between 300 and 100 K (Figure 4a). The grain size range that is blocked between 300 and 100 K was estimated to 30–50 nm, which is consistent with the measured average grain size (20–50 nm) and approximate SP proportions of 75% at room temperature and of 50% at 100 K. Magnetostatic interactions may additionally lower the SP/SD threshold to smaller sizes (Muxworthy, 2001; Muxworthy et al., 2013); stronger interactions at 100 K than at 300 K could, therefore, amplify the shift from SP to SD behavior.

4.6. Day Plot Mixing Trends

The Day plot distribution of our synthetic samples overlaps and continues the trend defined by natural SD-dominated greigite (Roberts et al., 2011) (Figure 4a), which points to a common SP endmember size close to 7 nm. This size roughly coincides with the inferred crystallite size for FeS, which was estimated to $\lesssim$5 nm after Step I and to 10 nm after Step II. Greigite forms by a solid-state transformation of FeS, so a similar particle size of the two phases should be expected. The SP endmember in our samples, thus, likely originates from transformation of single FeS crystallites whereas larger greigite grains may have developed from FeS aggregates. A similar SP endmember size for natural greigite from diverse locations reflects the typical nanoparticulate nature of its precursor FeS (Ohfuji & Rickard, 2006). The well-defined greigite trend along a single mixing line suggests that the smallest grains (5–10 nm) dominate the SP greigite fraction, which likely has a continuous size distribution, similarly as was reported for diagenetic SP-SD magnetite in remagetized carbonates (Jackson & Swanson-Hysell, 2012).

Overlap between the Day plot trends of SP-SD greigite and SD-MD magnetite (Dunlop, 2002) suggests that authigenic greigite with more than 40% SP contributions is difficult to distinguish from typical primary magnetite-bearing sediments. An overlap between SP-SD greigite and magnetite dominated sediments in the Day plot was reported, for example, in Quaternary marine sediments from the Gulf of Mexico (Fu et al., 2008).

4.7. Grain Arrangement and Magnetostatic Interactions

Magnetostatic interactions are primarily governed by the distance between magnetic particles. Higher concentration and/or local enrichment of magnetic particles within clusters, thus, lead to stronger interactions. The degree of interactions in a sample can be assessed by the vertical spread of its FORC distribution. FORC analysis indicate that the degree of interactions is similar for the matrix free (pure sulfide) sample #50-31 (Figure 4b) and for silt sample #100-10 (Figure 4c), in which the sulfide concentration is diluted to 0.1% by the sediment substrate. This implies that, for all our samples, interactions are independent of the greigite concentration and arise mainly from clustering. A dense clustering of the sulfides in our samples is inferred from the SEM images

of the non-matrix sample #50-31 (Figure 1b, final product). The magnetic fraction in a cluster can be expressed as the packing fraction, p, given by the net volume of magnetic particles relative to the total volume, when assuming a uniform cluster composition. In our samples, interactions increase with lower temperature (FWHM increase from 10 mT at 300 K to 24 mT at 100 K), consistent with an increase in the SD fraction, which was estimated to 16 ± 3 vol% at 300 K and 31 ± 2 vol% at 100 K (Section 4.2).

Numeric FORC models for uniaxial and cubic magnetite indicate that the vertical spread (FWHM of the B_u distribution) is proportional to the packing fraction and nearly independent of anisotropy type (Harrison & Lascu, 2014). Normalized by the mineral specific saturation magnetization, the FWHM is expected to be independent of magnetic mineralogy. With $\mu_0 M_s \approx 0.34$ T for greigite, our samples yield FWHM/$\mu_0 M_s$ values of 0.29 for 300 K and of 0.70 for 100 K. Comparison to the FWHM/$\mu_0 M_s$ values reported for modeled magnetite FORC distributions (Figure 9 of Harrison & Lascu, 2014) suggests packing fractions of $p_{300\,K} \approx 0.07$ (7 vol% magnetic fraction) and $p_{100\,K} \approx 0.27$ (27 vol%) in our samples.

General agreement between the estimated packing fraction of magnetic minerals and the SD greigite fraction relative to the total sulfide concentration further supports the interpretation that magnetostatic interactions arise predominantly from the proportion of SD greigite within densely packed sulfide clusters. Magnetostatic interactions can bias M_{rs}/M_s ratios to lower values and B_{cr}/B_c to higher values (Harrison & Lascu, 2014; Muxworthy, 2003). Hence, SD proportions inferred from the Day plot mixing lines likely underestimate the true SD contributions, particularly at 100 K. This could partially account for the discrepancy between a nearly fourfold difference in estimated packing fraction between 300 and 100 K versus a twofold difference in estimated SD-proportions. Similarly, magnetic interactions may explain why measured M_{rs}/M_s values of sedimentary greigite are generally lower than the expected value for SD grains dominated by cubic magnetocrystalline anisotropy (Roberts et al., 2011).

4.8. Sample Alteration in Air

When the samples were exposed to air after aging, yellow patches appeared in the sediment, which increased in number and size over time, thereby suggesting partial oxidation of Fe-sulfides to a yellow Fe-oxyhydroxide, possibly lepidocrocite and/or goethite. Observed changes in FORC distributions over a 12 hr period for sample #100-10 (Figure 4c) demonstrate that the greigite concentration (FORC amplitude) and magnetostatic interactions (vertical spread) decreased, and that thermal activation of the SD fraction increased (shift to lower B_c and higher B_u values). Room temperature FORC diagrams for sample #100-10 have a weak diagonal feature in the lower left half-plane, which is particularly expressed after oxidation. This feature, which is absent at 100 K and in both FORC diagrams of sample #50-3, resembles vortex state signatures associated with flux-closure among clustered SD grains (Egli, 2021). A gradual change in remanence and coercivity ratios marks a relative increase of the SP fraction (Figure 4a).

Taken together, these results suggest that oxidation led to an effective magnetic grain size reduction, where greigite particles were oxidized progressively to a non- or weakly magnetic phase, in accordance with a partial transformation to lepidocrocite and/or goethite. Reduced magnetic interactions point to a lower moment and/or to a larger distance between the remaining greigite particles, consistent with a grain size reduction by surface oxidation and an overall decrease in greigite concentration.

5. Conclusions

5.1. Greigite Formation and CRM Acquisition

We report a two-step synthesis method to transform lepidocrocite via mackinawite to greigite inside sealed non-magnetic vials. First lepidocrocite powder is transformed to nanoparticulate FeS in an anhydrous H_2S atmosphere at room temperature. FeS is then preferentially oxidized to greigite under aquatic conditions at 75°C via a solid-state transformation, presumably involving the loss of iron ($4FeS \rightarrow Fe_3S_4$) although the involved electron acceptor and the fate of the released iron are not identified.

Through bulk magnetic measurements during greigite growth in a defined magnetic field, the growth process and CRM acquisition can be monitored in real-time. Greigite was grown in different water saturated sediment substrates, which stabilized the greigite mechanically but did not influence the greigite growth kinetics. During

sample aging at 75°C, we observed a continuous increase in magnetic susceptibility and in CRM intensity. Nearly linear growth rates, which decreased by a factor of three after 2 hr, point to two distinct growth regimes. Two thirds of the precursor FeS transformed to greigite after 7 hr, leading to a final greigite concentration of ∼0.1 vol% in samples with a sediment matrix.

Using magnetic susceptibility growth rates at room temperature and 75°C, the activation energy for the FeS to greigite transformation was estimated at 78–90 kJ/mol, which agrees within uncertainty with previous estimates, based on direct analytical measurements (Hunger & Benning, 2007). Growth and particularly dissolution rates of greigite have been notoriously difficult to constrain partially due to a lack of pure greigite sample material and because direct in-situ phase analyses are difficult. Magnetic susceptibility measurements represent a valuable alternative to track in-situ greigite concentration in real-time. This indirect method is rapid, simple, and independent of the presence of a growth medium or other non-magnetic mineral phases like mackinawite and pyrite. Moreover, susceptibility can be calibrated with respect to greigite concentration by direct analysis of the studied material. Magnetic measurements, hence, could help to better constrain the solubility of greigite which is a relevant, yet poorly understood variable in sedimentary Fe-S cycles.

5.2. Greigite Preservation

Greigite is metastable with respect to pyrite when dissolved sulfide concentrations are high. Rock-magnetic studies, however, frequently identify greigite in marine sediments, where pyritization and pervasive diagenetic dissolution of detrital magnetite indicate high sulfide concentrations during diagenesis (Roberts et al., 2018; Roberts & Weaver, 2005). It remains unclear when, and under which conditions greigite accumulates, and how it becomes preserved. Our experiments indirectly confirm that the presence of trace amounts of aldehydes inhibit greigite dissolution and pyrite formation. This "sulfide-switch," originally reported by Rickard et al. (2001), could play a role in preserving greigite in sulfidic microenvironments associated with aldehyde-bearing organic matter. The microbial community involved in the sulfidation process may also influence greigite preservation, as greigite is stable in the presence of certain strains of hyperthermophilic archaea and magnetotactic bacteria (Gorlas et al., 2018; Posfai, 2006). Combining organic and sulfide chemistry with rock-magnetic methods in future studies may help to better understand the environmental conditions that promote greigite accumulation in marine sediments.

5.3. Magnetic Properties, Grain Size and Domain State

In our experiments, the SP-SD ratio, and hence the average grain size of greigite, remained constant as its concentration increased continuously at 75°C. Individual greigite grains reached a final size within minutes, consistent with a solid-state transformation where grain size is inherited from the precursor phase. This suggests that greigite grains form quasi-instantaneously, and that their size is fixed on geological timescales. Different domain states observed in natural sedimentary greigite may therefore reflect different paleoenvironmental growth conditions. However, progressively increasing greigite concentrations can enhance magnetostatic interactions, which potentially lowers the SP/SD threshold size, leading to more SD-like properties.

The average greigite grain size in our samples lies between 20 and 50 nm and spans the SP/SD threshold, in line with theoretical estimates for the greigite blocking volume. SD fractions of ∼25% at room temperature and ∼50% at 100 K were estimated. Comparison of M_S normalized FORC distributions of our samples to numerical FORC models (Harrison & Feinberg, 2008) suggests SD greigite packing fractions of 7% at room temperature and of 27% at 100 K.

Temperature-dependent Day plot distributions for our samples follow the trend of theoretical SP-SD mixing lines calculated for an SP greigite endmember of 7 nm, which is in accord with the crystallite size of the precursor FeS. Our data overlap with an empirical mixing trend defined by diverse greigite-bearing sediments, which together suggest a characteristic, common SP endmember size that likely dominates the SP greigite fraction volumetrically. An SP endmember between 5 and 10 nm agrees with the typical size of precipitated FeS. Our results suggests that the mixing model, based on binary SP and SD fractions, provides a realistic representation of the domain state and physical grain size of SP-SD greigite distributions. Although clustering and associated magnetostatic interactions in authigenic greigite potentially lead to underestimated SD proportions, the model can help quantify the grain size of sedimentary greigite, which is typically in a SP-SD state.

Data Availability Statement

All data mentioned in this study are available online at the open-access data repository Zenodo via https://doi.org/10.5281/zenodo.6521653.

Acknowledgments
We thank Dr. Erika Griesshaber for her support using the scanning electron microscope. This work was supported by the Deutsche Forschungsgemeinschaft (GI712/16-1). Editorial handling by Joshua Feinberg and helpful reviews by Andrew Roberts and one anonymous reviewer are greatly appreciated. Open Access funding enabled and organized by Projekt DEAL.

References

Chang, L., Roberts, A. P., Rowan, C. J., Tang, Y., Pruner, P., Chen, Q., & Horng, C.-S. (2009). Low-temperature magnetic properties of greigite (Fe_3S_4). *Geochemistry, Geophysics, Geosystems*, *10*(1). https://doi.org/10.1029/2008gc002276

Day, R., Fuller, M., & Schmidt, V. A. (1977). Hysteresis properties of titanomagnetites: Grain-size and compositional dependence. *Physics of the Earth and Planetary Interiors*, *13*(4), 260–267. https://doi.org/10.1016/0031-9201(77)90108-x

Dekkers, M. J., & Schoonen, M. A. A. (1996). Magnetic properties of hydrothermally synthesized greigite (Fe_3S_4)—I. Rock magnetic parameters at room temperature. *Geophysical Journal International*, *126*(2), 360–368. https://doi.org/10.1111/j.1365-246x.1996.tb05296.x

Dunlop, D. J. (2002). Theory and application of the Day plot (M_{rs}/M_s versus H_{cr}/H_c) 1. Theoretical curves and tests using titanomagnetite data. *Journal of Geophysical Research*, *107*(B3), 2056. https://doi.org/10.1029/2001jb000486

Egli, R. (2021). Magnetic characterization of geologic materials with first-order reversal curves. In F. Victorino & B. Dodrill (Eds.), *Magnetic measurement techniques for materials characterization* (pp. 455–604). Springer.

Egli, R. (2006). Theoretical considerations on the anhysteretic remanent magnetization of interacting particles with uniaxial anisotropy. *Journal of Geophysical Research*, *111*(B12S18). https://doi.org/10.1029/2006jb004577

Egli, R. (2013). VARIFORC: An optimized protocol for calculating non-regular first-order reversal curve (FORC) diagrams. *Global and Planetary Change*, *110*, 302–320. https://doi.org/10.1016/j.gloplacha.2013.08.003

Fu, Y., Dobeneck, T., von Franke, C., Heslop, D., & Kasten, S. (2008). Rock magnetic identification and geochemical process models of greigite formation in Quaternary marine sediments from the Gulf of Mexico (IODP Hole U1319A). *Earth and Planetary Science Letters*, *275*(3–4), 233–245. https://doi.org/10.1016/j.epsl.2008.07.034

Gorlas, A., Jacquemot, P., Guigner, J.-M., Gill, S., Forterre, P., & Guyot, F. (2018). Greigite nanocrystals produced by hyperthermophilic archaea of Thermococcales order. *PLoS One*, *13*(8), e0201549. https://doi.org/10.1371/journal.pone.0201549

Gražulis, S., Daškevič, A., Merkys, A., Chateigner, D., Lutterotti, L., Quirós, M., et al. (2012). Crystallography open Database (COD): An open-access collection of crystal structures and platform for world-wide collaboration. *Nucleic Acids Research*, *40*(D1), D420–D427. https://doi.org/10.1093/nar/gkr900

Hallam, D. F., & Maher, B. A. (1994). A record of reversed polarity carried by the iron sulphide greigite in British early Pleistocene sediments. *Earth and Planetary Science Letters*, *121*(1–2), 71–80. https://doi.org/10.1016/0012-821x(94)90032-9

Harrison, R. J., & Feinberg, J. M. (2008). FORCinel: An improved algorithm for calculating first-order reversal curve distributions using locally weighted regression smoothing. *Geochemistry, Geophysics, Geosystems*, *9*(5). https://doi.org/10.1029/2008gc001987

Harrison, R. J., & Lascu, I. (2014). FORCulator: A micromagnetic tool for simulating first-order reversal curve diagrams. *Geochemistry, Geophysics, Geosystems*, *15*(12), 4671–4691. https://doi.org/10.1002/2014gc005582

Hunger, S., & Benning, L. G. (2007). Greigite: A true intermediate on the polysulfide pathway to pyrite. *Geochemical Transactions*, *8*(1), 1. https://doi.org/10.1186/1467-4866-8-1

Igarashi, K., Yamamura, Y., & Kuwabara, T. (2016). Natural synthesis of bioactive greigite by solid–gas reactions. *Geochimica et Cosmochimica Acta*, *191*, 47–57. https://doi.org/10.1016/j.gca.2016.07.005

Jackson, M., & Swanson-Hysell, N. L. (2012). Rock magnetism of remagnetized carbonate rocks: Another look. *Geological Society, London, Special Publications*, *371*(1), 229–251. https://doi.org/10.1144/sp371.3

Jiang, W.-T., Horng, C.-S., Roberts, A. P., & Peacor, D. R. (2001). Contradictory magnetic polarities in sediments and variable timing of neoformation of authigenic greigite. *Earth and Planetary Science Letters*, *193*(1–2), 1–12. https://doi.org/10.1016/s0012-821x(01)00497-6

Jiang, Z., Liu, Q., Dekkers, M. J., Barrón, V., Torrent, J., & Roberts, A. P. (2016). Control of Earth-like magnetic fields on the transformation of ferrihydrite to hematite and goethite. *Scientific Reports*, *6*(1), 30395. https://doi.org/10.1038/srep30395

Just, J., Sagnotti, L., Nowaczyk, N. R., Francke, A., & Wagner, B. (2019). Recordings of fast paleomagnetic reversals in a 1.2 Ma greigite-rich sediment archive from Lake Ohrid, Balkans. *Journal of Geophysical Research: Solid Earth*, *124*(12), 12445–12464. https://doi.org/10.1029/2019jb018297

Larrasoaña, J. C., Roberts, A. P., Musgrave, R. J., Gràcia, E., Piñero, E., Vega, M., & Martínez-Ruiz, F. (2007). Diagenetic formation of greigite and pyrrhotite in gas hydrate marine sedimentary systems. *Earth and Planetary Science Letters*, *261*(3–4), 350–366. https://doi.org/10.1016/j.epsl.2007.06.032

Li, G., Zhang, B., Yu, F., Novakova, A. A., Krivenkov, M. S., Kiseleva, T. Y., et al. (2014). High-purity Fe_3S_4 greigite microcrystals for magnetic and electrochemical performance. *Chemistry of Materials*, *26*(20), 5821–5829. https://doi.org/10.1021/cm501493m

Muxworthy, A. (2003). Effect of magnetostatic interactions on the hysteresis parameters of single-domain and pseudo-single-domain grains. *Journal of Geophysical Research*, *108*(B11), 2517. https://doi.org/10.1029/2003jb002588

Muxworthy, A. R. (2001). Effect of grain interactions on the frequency dependence of magnetic susceptibility. *Geophysical Journal International*, *144*(2), 441–447. https://doi.org/10.1046/j.1365-246x.2001.00342.x

Muxworthy, A. R., Williams, W., Roberts, A. P., Winklhofer, M., Chang, L., & Pósfai, M. (2013). Critical single domain grain sizes in chains of interacting greigite particles: Implications for magnetosome crystals. *Geochemistry, Geophysics, Geosystems*, *14*(12), 5430–5441. https://doi.org/10.1002/2013gc004973

Nowaczyk, N. R., Liu, J., & Arz, H. W. (2020). Records of the laschamps geomagnetic polarity excursion from black sea sediments: Magnetite versus greigite, discrete sample versus U-channel data. *Geophysical Journal International*, *224*(2), 1079–1095. https://doi.org/10.1093/gji/ggaa506

Ohfuji, H., & Rickard, D. (2006). High resolution transmission electron microscopic study of synthetic nanocrystalline mackinawite. *Earth and Planetary Science Letters*, *241*(1–2), 227–233. https://doi.org/10.1016/j.epsl.2005.10.006

Pick, T., & Tauxe, L. (1991). Chemical remanent magnetization in synthetic magnetite. *Journal of Geophysical Research*, *96*(B6), 9925. https://doi.org/10.1029/91jb00706

Pike, C. R., Roberts, A. P., & Verosub, K. L. (1999). Characterizing interactions in fine magnetic particle systems using first order reversal curves. *Journal of Applied Physics*, *85*(9), 6660–6667. https://doi.org/10.1063/1.370176

Pike, C. R., Roberts, A. P., & Verosub, K. L. (2001). First-order reversal curve diagrams and thermal relaxation effects in magnetic particles. *Geophysical Journal International*, *145*(3), 721–730. https://doi.org/10.1046/j.0956-540x.2001.01419.x

Posfai, M. (2006). Sulfides in biosystems. *Reviews in Mineralogy and Geochemistry*, *61*(1), 679–714. https://doi.org/10.2138/rmg.2006.61.13

Rickard, D. (1995). Kinetics of FeS precipitation: Part 1. Competing reaction mechanisms. *Geochimica et Cosmochimica Acta*, *59*(21), 4367–4379. https://doi.org/10.1016/0016-7037(95)00251-t

Rickard, D. (2012). Sedimentary sulfides. In D. T. Rickard (Ed.), *Sulfidic sediments and sedimentary rocks* (Vol. 65, pp. 543–604). Elsevier Science Ltd.

Rickard, D., Butler, I. B., & Oldroyd, A. (2001). A novel iron sulphide mineral switch and its implications for Earth and planetary science. *Earth and Planetary Science Letters*, *189*(1–2), 85–91. https://doi.org/10.1016/s0012-821x(01)00352-1

Roberts, A. P., Chang, L., Rowan, C. J., Horng, C.-S., & Florindo, F. (2011). Magnetic properties of sedimentary greigite (Fe_3S_4): An update. *Reviews of Geophysics*, *49*(1), RG1002. https://doi.org/10.1029/2010rg000336

Roberts, A. P., Jiang, W.-T., Florindo, F., Horng, C.-S., & Laj, C. (2005). Assessing the timing of greigite formation and the reliability of the Upper Olduvai polarity transition record from the Crostolo River, Italy. *Geophysical Research Letters*, *32*(5), L05307. https://doi.org/10.1029/2004gl022137

Roberts, A. P., Liu, Q., Rowan, C. J., Chang, L., Carvallo, C., Torrent, J., & Horng, C.-S. (2006). Characterization of hematite (α-Fe_2O_3), goethite (α-FeOOH), greigite (Fe_3S_4), and pyrrhotite (Fe_7S_8) using first-order reversal curve diagrams. *Journal of Geophysical Research*, *111*(B12). https://doi.org/10.1029/2006jb004715

Roberts, A. P., & Weaver, R. (2005). Multiple mechanisms of remagnetization involving sedimentary greigite (Fe_3S_4). *Earth and Planetary Science Letters*, *231*(3–4), 263–277. https://doi.org/10.1016/j.epsl.2004.11.024

Roberts, A. P., Zhao, X., Harrison, R. J., Heslop, D., Muxworthy, A. R., Rowan, C. J., et al. (2018). Signatures of reductive magnetic mineral diagenesis from unmixing of first-order reversal curves. *Journal of Geophysical Research: Solid Earth*, *123*(6), 4500–4522. https://doi.org/10.1029/2018jb015706

Ron, H., Nowaczyk, N. R., Frank, U., Schwab, M. J., Naumann, R., Striewski, B., & Agnon, A. (2007). Greigite detected as dominating remanence carrier in late pleistocene sediments, lisan formation, from lake kinneret (sea of galilee), Israel. *Geophysical Journal International*, *170*(1), 117–131. https://doi.org/10.1111/j.1365-246x.2007.03425.x

Rowan, C. J., & Roberts, A. P. (2006). Magnetite dissolution, diachronous greigite formation, and secondary magnetizations from pyrite oxidation: Unravelling complex magnetizations in Neogene marine sediments from New Zealand. *Earth and Planetary Science Letters*, *241*(1–2), 119–137. https://doi.org/10.1016/j.epsl.2005.10.017

Sagnotti, L., Roberts, A. P., Weaver, R., Verosub, K. L., Florindo, F., Pike, C. R., et al. (2005). Apparent magnetic polarity reversals due to remagnetization resulting from late diagenetic growth of greigite from siderite. *Geophysical Journal International*, *160*(1), 89–100. https://doi.org/10.1111/j.1365-246x.2005.02485.x

Scherrer, P. (1912). Bestimmung der inneren Struktur und der Größe von Kolloidteilchen mittels Röntgenstrahlen. In R. Zsigmondy (Ed.), *Kolloidchemie ein lehrbuch* (pp. 387–409). Springer.

Schneider, C. A., Rasband, W. S., & Eliceiri, K. W. (2012). NIH image to ImageJ: 25 years of image analysis. *Nature Methods*, *9*(7), 671–675. https://doi.org/10.1038/nmeth.2089

Schoonen, M. A. (2004). Mechanisms of sedimentary pyrite formation. In J. P. Amend, K. J. Edwards, & T. W. Lyons (Eds.). *Sulfur biogeochemistry - past and present*. Geological Society of America. (Vol. 379, pp. 117–134).

Stokking, L. B., & Tauxe, L. (1990). Properties of chemical remanence in synthetic hematite: Testing theoretical predictions. *Journal of Geophysical Research*, *95*(B8), 12639. https://doi.org/10.1029/jb095ib08p12639

Till, J. L., Guyodo, Y., Lagroix, F., Ona-Nguema, G., & Brest, J. (2014). Magnetic comparison of abiogenic and biogenic alteration products of lepidocrocite. *Earth and Planetary Science Letters*, *395*, 149–158. https://doi.org/10.1016/j.epsl.2014.03.051

Valdez-Grijalva, M. A., Nagy, L., Muxworthy, A. R., Williams, W., & Fabian, K. (2018). The magnetic structure and palaeomagnetic recording fidelity of sub-micron greigite (Fe_3S_4). *Earth and Planetary Science Letters*, *483*, 76–89. https://doi.org/10.1016/j.epsl.2017.12.015

White, L. M., Bhartia, R., Stucky, G. D., Kanik, I., & Russell, M. J. (2015). Mackinawite and greigite in ancient alkaline hydrothermal chimneys: Identifying potential key catalysts for emergent life. *Earth and Planetary Science Letters*, *430*, 105–114. https://doi.org/10.1016/j.epsl.2015.08.013

Wilkin, R. T., & Barnes, H. L. (1996). Pyrite formation by reactions of iron monosulfides with dissolved inorganic and organic sulfur species. *Geochimica et Cosmochimica Acta*, *60*(21), 4167–4179. https://doi.org/10.1016/s0016-7037(97)81466-4

Winklhofer, M., Chang, L., & Eder, S. H. K. (2014). On the magnetocrystalline anisotropy of greigite (Fe_3S_4). *Geochemistry, Geophysics, Geosystems*, *15*(4), 1558–1579. https://doi.org/10.1002/2013gc005121